Available online at www.sciencedirect.com
ScienceDirect
Physica B 394 (2007) 357–362
PHYSICA B
www.elsevier.com/locate/physb

Complex bounds and microstructural recovery from measurements of sea ice permittivity

A. Gully[a], L.G.E. Backstrom[b], H. Eicken[b], K.M. Golden[a,*]

[a]Department of Mathematics, University of Utah, 155 S 1400 E RM 233, Salt Lake City, UT 84112-0090, USA
[b]Geophysical Institute, University of Alaska, P.O. Box 757320, 903 Koyukuk Drive, Fairbanks, AK 99775-7320, USA

Abstract

Sea ice is a porous composite of pure ice with brine, air, and salt inclusions. The polar sea ice packs play a key role in the earth's ocean-climate system, and they host robust algal and bacterial communities that support the Arctic and Antarctic ecosystems. Monitoring the sea ice packs on global or regional scales is an increasingly important problem, typically involving the interaction of an electromagnetic wave with sea ice. In the quasistatic regime where the wavelength is much longer than the composite microstructural scale, the electromagnetic behavior is characterized by the effective complex permittivity tensor $\boldsymbol{\varepsilon}^*$. In assessing the impact of climate change on the polar sea ice covers, current satellites and algorithms can predict ice extent, but the thickness distribution remains an elusive, yet most important feature. In recent years, electromagnetic induction devices using low frequency waves have been deployed on ships, helicopters and planes to obtain thickness data. Here we compare two sets of theoretical bounds to extensive outdoor tank and *in situ* field data on $\boldsymbol{\varepsilon}^*$ at 50 MHz taken in the Arctic and Antarctic. The sea ice is assumed to be a two phase composite of ice and brine with known constituent permittivities. The first set of bounds assumes only knowledge of the brine volume fraction or porosity, and the second set further assumes statistical isotropy of the microstructure. We obtain excellent agreement between theory and experiment, and are able to observe the apparent violation of the isotropic bounds as the vertically oriented microstructure becomes increasingly connected for higher porosities. Moreover, these bounds are inverted to obtain estimates of the porosity from the measurements of $\boldsymbol{\varepsilon}^*$. We find that the temporal variations of the reconstructed porosity, which is directly related to temperature, closely follow the actual behavior.

PACS: 92.10.Rw; 77.84.Lf; 77.22.Ch; 02.30.Zz; 92.70.Mn; 93.85.Jk; 93.30.Li; 93.30.Ca

Keywords: Sea ice; Complex permittivity; Bounds; Microstructural inversion; Sea ice thickness

1. Introduction

Covering approximately 7–10% of the earth's ocean surface, sea ice is an important component of the global climate system and is an indicator of climatic change [1]. During the winter months in the Arctic and Antarctic, the extensive sea ice packs serve as the boundary layer which mediates the exchange of heat, moisture, and momentum between the atmosphere and ocean [2,3]. In fact, the sea ice pack surrounding Antarctica during winter has greater surface area than the continent itself. The vast expanses of sea ice also serve as a habitat for rich microbial communities which live in the brine microstructure of porous sea ice [2,4,5]. These algal and bacterial communities are primary providers for the complex food webs in the polar oceans.

Because of the global nature of monitoring the earth's sea ice packs, large scale information is usually obtained via remote sensing from platforms on satellites, aircraft and ships [6–10]. The physics underlying the problem of remotely sensing sea ice concerns the interaction of an electromagnetic wave with a polycrystalline composite of four components: pure ice, brine inclusions, air pockets, and solid salt deposits [11,12]. For this study we will ignore the air and solid salt phases and view sea ice as a two phase

*Corresponding author.
E-mail addresses: c-gyas@math.utah.edu (A. Gully), larsg@gi.alaska.edu (L.G.E. Backstrom), hajo.eicken@gi.alaska.edu (H. Eicken), golden@math.utah.edu (K.M. Golden).

0921-4526/$ - see front matter © 2007 Elsevier B.V. All rights reserved.
doi:10.1016/j.physb.2006.12.067

composite of ice with brine inclusions. One of the grand challenges of sea ice remote sensing is to accurately recover the thickness distribution of the pack. Assessing the impact of global warming on the polar regions involves monitoring not only the ice extent, but the ice volume, which requires knowledge of ice thickness. Recently there has been increasing interest in using low frequency electromagnetic induction devices to estimate sea ice thickness [13]. Electromagnetic fields with wavelengths on the scale of meters are used to probe the air–ice–ocean interface and estimate the thickness of the ice layer. Since typical sizes of the brine inclusions are on the sub-millimeter scale, the electromagnetic behavior of the sea ice can be treated using the quasistatic approximation. Then the sea ice can be characterized electromagnetically via the effective complex permittivity tensor $\boldsymbol{\varepsilon}^*$. There has been considerable work in the past on estimating and bounding $\boldsymbol{\varepsilon}^*$ for sea ice, particularly in the microwave region [8,14–21].

Here, we compare theoretical bounds on the principal components of $\boldsymbol{\varepsilon}^*$ with extensive outdoor tank and *in situ* data on $\boldsymbol{\varepsilon}^*$ at 50 MHz, consisting of thousands of measurements, taken with a capacitance probe [22]. In particular, we compare the low frequency measurements with the Bergman–Milton bounds [23–25] for the complex permittivity of a two phase composite with known constituent permittivities ε_1 and ε_2 and volume fractions p_1 and p_2. There are two types of these bounds which we employ. The first type assumes only the permittivity and volume fraction information, and are known as the complex elementary or arithmetic and harmonic mean bounds. The second type further assumes statistical isotropy in the composite microstructure, and are known as the complex Hashin–Shtrikman bounds [26].

All the data considered are situated well inside the complex elementary bounds. However, there are naturally occurring anisotropies in the brine microstructure, such as its preferred vertical orientation [11,12], which becomes more pronounced above the critical brine volume fraction of about 5% where the brine phase percolates [27]. Also, preferred azimuthal alignment of the c-axes of individual crystals within the horizontal plane has long been observed in the Arctic [28], and was present in the Arctic sea ice whose permittivity was measured in one of the data sets considered here [22]. Preferred c-axis alignment is attended by anistropy in the brine microstructure, and anisotropic behavior of the complex permittivity within the horizontal plane [16]. Comparing the different data sets with the isotropic bounds yields interesting and useful insights about sea ice microstructure, its evolution with temperature, and its electromagnetic properties. We also invert the complex bounds to obtain rigorous estimates of the brine volume fraction from the permittivity data [9,29–31].

2. Forward bounds for the effective complex permittivity

Let us briefly describe the analytic continuation method for studying the effective properties of composite materials [20,23–25]. Let $\varepsilon(x,\omega)$ be a spatially stationary random field in $x \in \mathbb{R}^d$ and $\omega \in \Omega$, where Ω is the set of all realizations of the random medium, which represents the local values of the complex permittivity. We assume $\varepsilon(x,\omega)$ for 50 MHz takes the values $\varepsilon_1 = 63.3 + i1930$ in brine and $\varepsilon_2 = 3.06$ in ice [22], and write $\varepsilon(x,\omega) = \varepsilon_1\chi_1(x,\omega) + \varepsilon_2\chi_2(x,\omega)$, where χ_j is the characteristic function of medium $j = 1, 2$, which equals one for all realizations $\omega \in \Omega$ having medium j at x, and equals zero otherwise. Let $E(x,\omega)$ and $D(x,\omega)$ be the stationary random electric and displacement fields satisfying the constitutive law $D(x,\omega) = \varepsilon(x,\omega)E(x,\omega)$ and the equations

$$\nabla \cdot D(x,\omega) = 0, \quad \nabla \times E(x,\omega) = 0, \tag{1}$$

with $\langle E(x,\omega)\rangle = e_k$, where e_k is a unit vector in the kth direction for some $k = 1, \ldots, d$, and $\langle\cdot\rangle$ means an ensemble average over Ω or spatial average over all of $\mathbb{R}^d$.

The effective complex permittivity tensor $\boldsymbol{\varepsilon}^*$ is defined by

$$\langle D\rangle = \boldsymbol{\varepsilon}^*\langle E\rangle. \tag{2}$$

For simplicity, we focus on one diagonal coefficient $\varepsilon^* = \varepsilon^*_{kk}$. Due to the homogeneity of effective parameters, $\varepsilon^*(\lambda\varepsilon_1, \lambda\varepsilon_2) = \lambda\varepsilon^*(\varepsilon_1, \varepsilon_2)$, ε^* depends only on the ratio $h = \varepsilon_1/\varepsilon_2$, and we define $m(h) = \varepsilon^*/\varepsilon_2$. The two main properties of $m(h)$ are that it is analytic off $(-\infty, 0]$ in the h-plane, and that it maps the upper half plane to the upper half plane [25,32], so that it is an example of a Herglotz, or Stieltjes function. The key step in the analytic continuation method is obtaining an integral representation for ε^*.

It is more convenient to work with the function [32] $F(s) = 1 - m(h)$, where $s = 1/(1-h)$, which is analytic off $[0, 1]$ in the s-plane. It was proven [25,32] that $F(s)$ has the representation

$$F(s) = \int_0^1 \frac{\mathrm{d}\mu(z)}{s - z}, \quad s \notin [0, 1], \tag{3}$$

where μ is a positive measure on $[0, 1]$. Formula (3) separates the parameter information in s from information about the mixture geometry contained in μ, a spectral measure of the operator $\Gamma\chi_1$, where $\Gamma = \nabla(-\Delta)^{-1}\nabla\cdot$. Statistical assumptions about the geometry are incorporated into μ via its moments $\mu_n = \int_0^1 z^n \,\mathrm{d}\mu(z)$, which can be calculated from the correlation functions of the random medium, with $\mu_n = (-1)^n\langle\chi_1[(\Gamma\chi_1)^n e_k]\cdot e_k\rangle$. For the complex elementary bounds it is assumed that we know only $\mu_0 = p_1$, and if the medium is statistically isotropic we know $\mu_1 = p_1p_2/d$ as well.

Bounds on ε^*, or $F(s)$, are obtained by fixing s in Eq. (3), varying over admissible measures μ (or admissible geometries), such as those that satisfy only $\mu_0 = p_1$, and finding the corresponding range of values of $F(s)$ in the complex plane. Two types of bounds on ε^* are obtained. The first bound R_1 assumes only that the relative volume fractions p_1 and $p_2 = 1 - p_1$ of the ice and brine are known, with $\mu_0 = p_1$ satisfied. In this case, the admissible set of measures forms a compact, convex set $\mathscr{M}_0$. Since F is a linear functional of μ, the extreme values of F are attained

by extreme points of $\mathscr{M}_0$, which are the Dirac point measures $p_1\delta_z$. The values of F lie inside the region R_1 bounded by circular arcs, one of which is parameterized in the F-plane by

$$C_1(z) = \frac{p_1}{s - z}, \quad 0 \leqslant z \leqslant p_2. \tag{4}$$

To display the other arc, we use the auxiliary function [33] $E(s) = 1 - \varepsilon_1/\varepsilon^*$, which is a Herglotz function like $F(s)$, analytic off $[0, 1]$. Then in the E-plane, we can parameterize the other circular boundary of R_1 by

$$\hat{C}_1(z) = \frac{p_2}{s - z}, \quad 0 \leqslant z \leqslant p_1. \tag{5}$$

In the common ε^*-plane, R_1 has vertices $V_1 = \varepsilon_1/(1 - \hat{C}_1(0)) = (p_1/\varepsilon_1 + p_2/\varepsilon_2)^{-1}$ and $W_1 = \varepsilon_2(1 - C_1(0)) = p_1\varepsilon_1 + p_2\varepsilon_2$. This region collapses to the interval $(p_1/\varepsilon_1 + p_2/\varepsilon_2)^{-1} \leqslant \varepsilon^* \leqslant p_1\varepsilon_1 + p_2\varepsilon_2$ when ε_1 and ε_2 are real, which are the arithmetic (upper) and harmonic (lower) mean bounds. The complex elementary bounds in Eqs. (4) and (5) are optimal and can be attained by coated ellipsoidal geometries as the aspect ratio varies.

If the material is further assumed to be statistically isotropic, i.e., $\varepsilon^*_{ik} = \varepsilon^*\delta_{ik}$, then $\mu_1 = p_1p_2/d$ must be satisfied as well. A convenient way of including this information [33] is to use the function $F_1(s) = 1/p_1 - 1/(sF(s))$, which is, again, a Herglotz function with a representation similar to Eq. (3) with a measure μ^1. The constraint $\mu_1 = p_1p_2/d$ on $F(s)$ is then transformed to a restriction of only the mass, or zeroth moment μ^1_0 of μ^1, with $\mu^1_0 = p_2/p_1d$. Applying the same procedure as for R_1 yields a region R_2, whose boundaries are again circular arcs. In the F-plane, one of these arcs is parameterized by

$$C_2(z) = \frac{p_1(s - z)}{s(s - z - p_2/d)}, \quad 0 \leqslant z \leqslant (d - 1)/d. \tag{6}$$

In the E-plane, the other arc is parameterized by

$$\hat{C}_2(z) = \frac{p_2(s - z)}{s(s - z - p_1(d - 1)/d)}, \quad 0 \leqslant z \leqslant 1/d. \tag{7}$$

In the ε^*-plane, R_2 has vertices $V_2 = \varepsilon_2(1 - C_2(0))$ and $W_2 = \varepsilon_1/(1 - \hat{C}_2(0))$, and collapses to the intervals

$$\varepsilon^* \geqslant \varepsilon_2 + p_1 \Big/ \left(\frac{1}{\varepsilon_1 - \varepsilon_2} + \frac{p_2}{d\varepsilon_2}\right), \tag{8}$$

$$\varepsilon^* \leqslant \varepsilon_1 + p_2 \Big/ \left(\frac{1}{\varepsilon_2 - \varepsilon_1} + \frac{p_1}{d\varepsilon_1}\right), \tag{9}$$

when ε_1 and ε_2 are real with $\varepsilon_1 \geqslant \varepsilon_2$, which are the Hashin-Shtrikman bounds [26]. When $\varepsilon_1 \leqslant \varepsilon_2$, the sequence of inequalities is reversed. The vertices V_2 and W_2 (which correspond to the expressions in (8)), are attained by the Hashin-Shtrikman coated sphere geometries.

3. Inverse bounds for structural parameters

The objective of inverse bounds is to use data about the electromagnetic response of sea ice to recover information about its structural parameters, in particular its brine volume fraction $p_1 = \phi$, or porosity. The porosity ϕ can be written as a function of the bulk ice salinity S and temperature T, as derived by semi-empirical approaches from the sea ice phase relations [11,12]. Given salinity information, for example, inverting for porosity yields temperature information. The inverse method [9,29–31] we use here yields intervals of uncertainty for the brine volume fraction ϕ. Given an observed value of the complex permittivity ε^*, ϕ is increased until the value of ε^* touches one boundary of the region R_1 described in the previous section, and is then decreased until the value touches the other boundary. This procedure gives a range of values $\phi^\ell_1 \leqslant \phi \leqslant \phi^u_1$, with

$$\phi^\ell_1 = |f|^2 \frac{\mathrm{Im}(\bar{s})}{\mathrm{Im}(f)}, \quad \phi^u_1 = 1 - \frac{|g|^2\mathrm{Im}(\bar{t})}{\mathrm{Im}(g)}, \tag{10}$$

where f is the known value of $F(s)$ and g is the known value of $G(t) = 1 - \varepsilon^*/\varepsilon_1$ with $t = 1 - s$. If the material is further assumed to be statistically isotropic, second order inverse bounds $\phi^\ell_2 \leqslant \phi \leqslant \phi^u_2$ can be obtained as well [29].

4. Comparison of theoretical bounds with measurements

Now we compare three extensive sets of data [22] on the complex permittivity of sea ice with the forward and inverse bounds. Measurements were taken in land-fast ice in the Chukchi Sea near Barrow, Alaska (14,004 data points) and in McMurdo Sound, Antarctica (2382 data points) and in artificial, young sea ice in an outdoor tank in Fairbanks, Alaska (6403 data points). The permittivity was measured by deploying an array of Stevens Water Monitoring Systems Hydraprobes. Each Hydraprobe is a coaxial probe with a central tine surrounded by three equally spaced outer tines, aligned horizontally, as shown in the photo inset in Fig. 1. The three outer tines are held at ground potential, and a voltage is applied to the central tine at 50 MHz frequency, resulting in a circularly polarized wave with electric field predominantly in the plane perpendicular to the tines. The complex permittivity measured by the probe represents an average of the components of $\boldsymbol{\varepsilon}^*$ in this plane. The porosities have been calculated from the measured *in situ* temperature and bulk salinity, via the known phase relations for standard sea ice [11,12], with details provided in Ref. [22]. The bulk ice salinity has been measured at regular intervals, with interpolation between these measurements in time based on a desalination model [22].

In Fig. 1 the full data set for the Fairbanks ice tank experiment is displayed along with a series of regions $R_1(\phi)$, for the indicated values of the brine porosity ϕ. The data have been grouped into intervals of porosity, $[0.02, 0.03]$, $[0.03, 0.04], \ldots, [0.08, 0.09]$, with a different

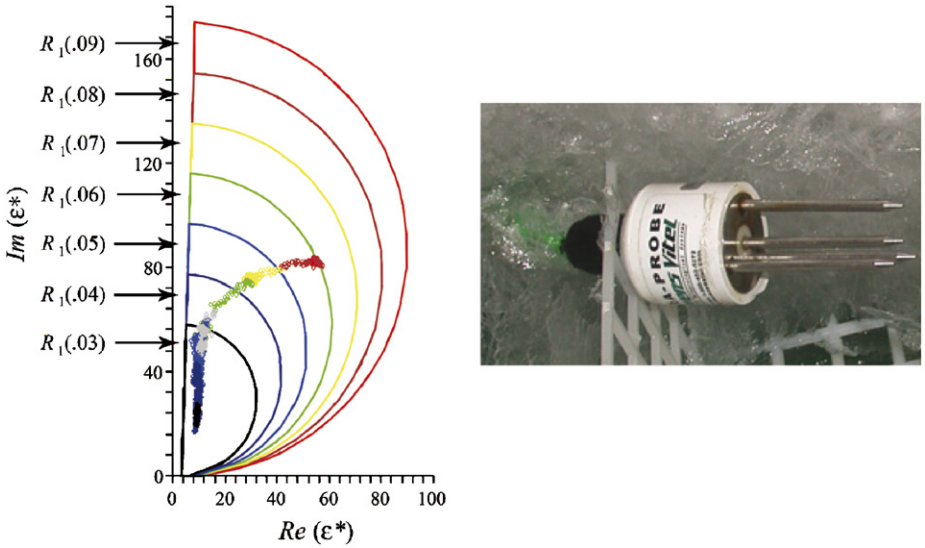

Fig. 1. Comparison of data on the complex permittivity at 50 MHz of sea ice grown in an ice tank with the elementary bounds. Data in a brine porosity interval signified by a given color lies inside the region of the same color. The data colored grey have porosities in the interval [0.049, 0.051]. The capacitance probe is shown on the right.

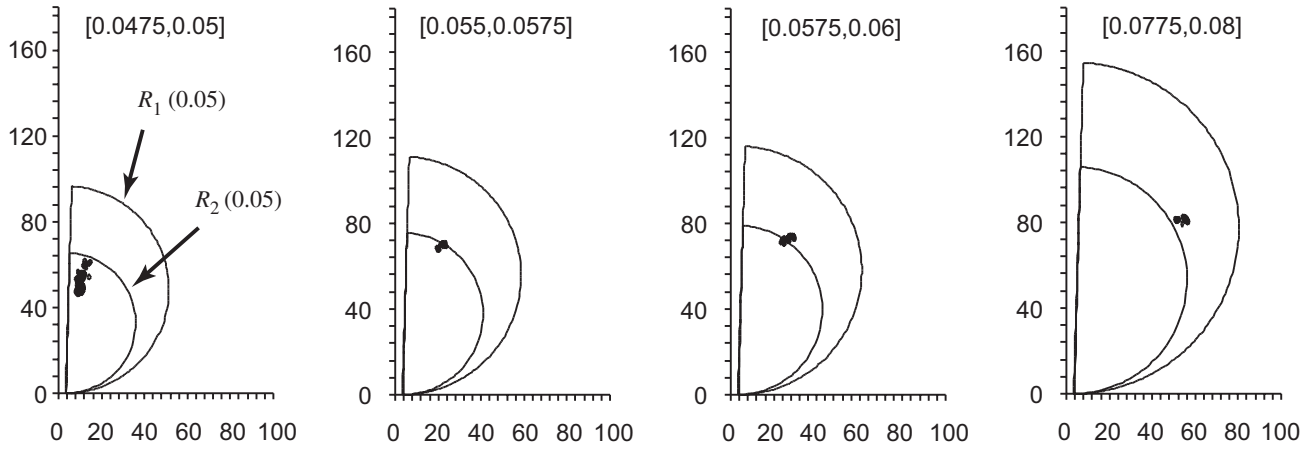

Fig. 2. Comparison of ice tank data on the complex permittivity of sea ice at 50 MHz with the elementary and isotropic bounds. The isotropic bounds are violated as brine volume increases in this case.

color for each interval. The corresponding elementary bound has the same color. All the data in each interval lie inside the corresponding bound. The data marked with the grey color lies in the porosity interval [0.049, 0.051], which corresponds to the percolation threshold of about 5% conjectured in Ref. [27]. In Fig. 2 we display a series of comparisons of data in the porosity intervals shown, with corresponding elementary bounds $R_1(\phi_{\max})$ and the isotropic bounds $R_2(\phi_{\max})$, where $\phi_{\max}$ is the largest porosity in each interval. The development of anisotropy in the dielectric measurements, or violation of the isotropic bounds, as brine volume increases through 5%, is consistent with an increasingly connected and vertically elongated brine microstructure. This behavior in the data would likely be accentuated if the electric field were oriented predominantly in the vertical direction.

In Fig. 3(a) and (b), two subsets of the Barrow data set, with porosities in the indicated intervals, are compared with the elementary and isotropic bounds for the middle porosity value within each interval. All the data over the entire range of porosities [0.05, 0.15] lie within both regions. Given that the entire range of porosities exceeds the critical value of 5%, one might expect the data to display marked anisotropy and perhaps violate the isotropic bound. However, in the fast-ice where the probes were deployed, there was a preferred azimuthal c-axis orientation within the horizontal plane, paralleling the predominant current direction along the shore, as in Ref. [28]. In such cases, it has been shown [16] how the permittivity in the horizontal plane, particularly at low frequencies, can be strongly enhanced in the direction perpendicular to the preferred c-axis direction, due to alignment of the brine microstructure. The probes in the experiment were aligned so

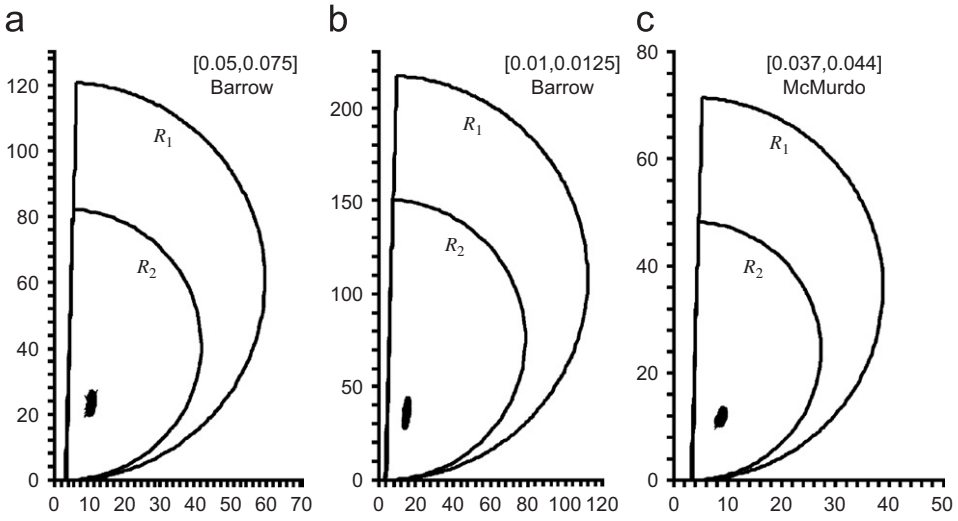

Fig. 3. In (a) and (b), complex permittivity data taken in the Chukchi Sea off Barrow, Alaska, for porosities in the indicated ranges, fall within both the elementary and isotropic bounds. In (c), permittivity data taken in McMurdo Sound, Antarctica over the indicated porosity interval, also fall within both bounds.

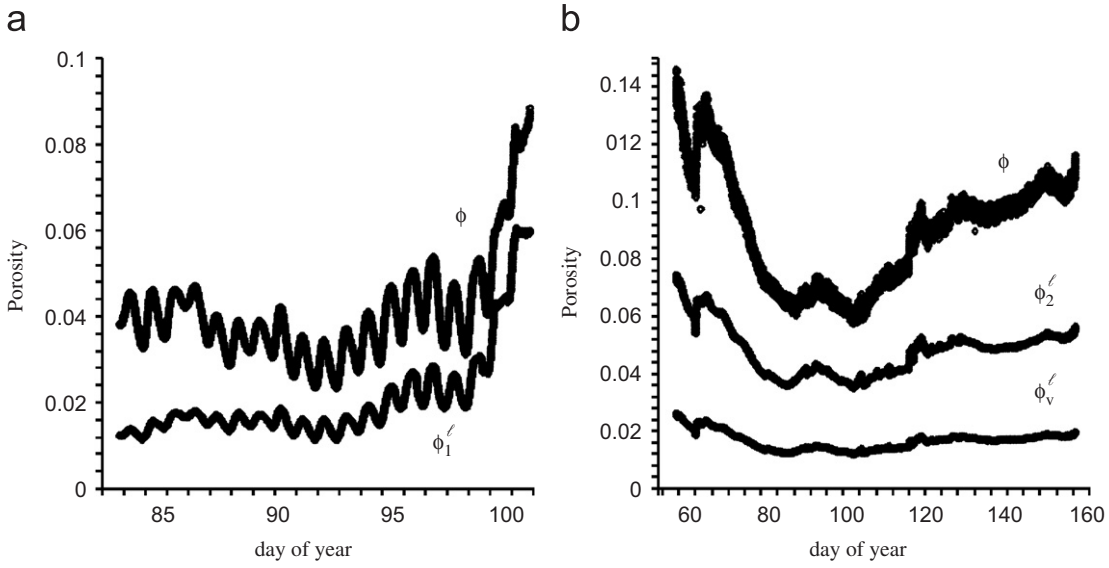

Fig. 4. Comparison of the actual brine porosity ϕ with time to the inverse lower bounds, for the ice tank data in (a) and for the Barrow data in (b).

that the tines were parallel to the preferred c-axis direction, with the electric field in the perpendicular, vertical plane. Thus, with alignment and elongation of the brine microstructure in both the vertical and horizontal directions within this plane, the data appears isotropic for this specific experimental configuration, and lies within the isotropic bounds. In Fig. 3(c), all the McMurdo data, with porosities in a tight range less than 5%, lie inside the elementary and isotropic bounds.

In Fig. 4(a), the actual brine porosity $\phi(t)$ as a function of time t for the ice tank experiment is compared with the lower inverse bound ϕ_1^{ℓ}. Due to the high contrast in the materials, the corresponding upper bound is quite large and currently provides little information. We see that the actual data lies above the lower bound, and that the variations in the reconstructed lower bound follow the variations in the actual porosity. In Fig. 4(b), the actual brine porosity for the Barrow data is compared with the lower inverse bounds ϕ_1^{ℓ} and ϕ_2^{ℓ}. Again, the inverse bounds are obeyed, and the variations in $\phi(t)$ are reflected in the behavior of the reconstructed functions.

5. Conclusions

We have compared extensive data sets on the complex permittivity of artificial and natural sea ice at 50 MHz with the Bergman–Milton bounds, and in general obtained excellent agreement. Comparison of the data with the isotropic forward bounds, in particular, and observing the development of possible violations of these bounds, serves almost as an inverse method for recovering interesting information about the microstructure. Finally, we inverted the permittivity data to obtain bounds on the brine porosity, again with good agreement. The close correlation between the time dependence of the actual brine porosity and the reconstructed bounds suggests that by finding tighter inverse bounds one could very closely reconstruct the actual brine porosity via capacitance measurements. We expect that these findings will aid in the recovery of ice type and property information from remote sensing and nondestructive, *in situ* measurements, potentially contributing to the indirect derivation of ice thickness information.

Acknowledgments

We are grateful for the support provided by the Division of Atmospheric Sciences and the Division of Mathematical Sciences at the National Science Foundation, through the Collaboration in Mathematical Geosciences (CMG) Program. Adam Gully gratefully acknowledges the support of the NSF Research Experiences for Undergraduates (REU) Program and an NSF VIGRE graduate fellowship.

References

[1] N. Untersteiner, Verhöff. Univ. Innsbruck 178 (1990) 209.
[2] D.N. Thomas, G.S. Dieckmann (Eds.), Sea Ice: An Introduction to its Physics, Chemistry, Biology and Geology, Blackwell, Oxford, 2003.
[3] M.O. Jeffries (Ed.), Antarctic Sea Ice: Physical Processes, Interactions and Variability, American Geophysical Union, Washington, DC, 1998.
[4] C.H. Fritsen, V.I. Lytle, S.F. Ackley, C.W. Sullivan, Science 266 (1994) 782.
[5] M.P. Lizotte, K.R. Arrigo (Eds.), Antarctic Sea Ice: Biological Processes, Interactions and Variability, American Geophysical Union, Washington, DC, 1998.
[6] R.A. Shuchman, R.G. Onstott, Remote sensing of the polar oceans, in: W.O. Smith (Ed.), Polar Oceanography, Part A, Physical Science, Academic Press, 1990, pp. 123–169.
[7] F.D. Carsey (Ed.), Microwave Remote Sensing of Sea Ice, Geophysical Monograph, vol. 68, American Geophysical Union, Washington, DC, 1992.
[8] D.P. Winebrenner, J. Bredow, A.K. Fung, M.R. Drinkwater, S. Nghiem, A.J. Gow, D.K. Perovich, T.C. Grenfell, H.C. Han, J.A. Kong, J.K. Lee, S. Mudaliar, R.G. Onstott, L. Tsang, R.D. West, Microwave sea ice signature modeling, in: F.D. Carsey (Ed.), Microwave Remote Sensing of Sea Ice, Geophysical Monograph, vol. 68, American Geophysical Union, 1992, pp. 137–175.
[9] K.M. Golden, D. Borup, M. Cheney, E. Cherkaeva, M.S. Dawson, K.H. Ding, A.K. Fung, D. Isaacson, S.A. Johnson, A.K. Jordan, J.A. Kong, R. Kwok, S.V. Nghiem, R.G. Onstott, J. Sylvester, D.P. Winebrenner, I. Zabel, IEEE Trans. Geosci. Remote Sensing 36 (5) (1998) 1675.
[10] D. Lubin, R. Massom, Polar Remote Sensing, Atmosphere and Oceans, vol. I, Springer, New York, 2006.
[11] W.F. Weeks, S.F. Ackley, The growth, structure and properties of sea ice, in: N. Untersteiner (Ed.), The Geophysics of Sea Ice, Plenum Press, New York, 1986, pp. 9–164.
[12] H. Eicken, Growth microstructure and properties of sea ice, in: D.N. Thomas, G.S. Dieckmann (Eds.), Sea Ice: An Introduction to its Physics, Chemistry, Biology and Geology, Blackwell, Oxford, 2003, pp. 22–81.
[13] J.E. Reid, A.P. Worby, J. Vrbancich, A.I.S. Munro, Geophysics 68 (5) (2003) 1537.
[14] A. Stogryn, IEEE Trans. Geosci. Remote Sensing GE-25 (2) (1985) 147.
[15] M.R. Vant, R.O. Ramseier, V. Makios, J. Appl. Phys. 49 (3) (1978) 1264.
[16] K.M. Golden, S.F. Ackley, J. Geophys. Res. (Oceans) 86 (C9) (1981) 8107.
[17] S.A. Arcone, A.J. Gow, S. McGrew, J. Geophys. Res. (Oceans) 91 (C12) (1986) 14281.
[18] A.H. Sihvola, J.A. Kong, IEEE Trans. Geosci. Remote Sensing 26 (4) (1988) 420.
[19] K. Golden, J. Geophys. Res. (Oceans) 100 (C7) (1995) 13,699.
[20] K.M. Golden, The interaction of microwaves with sea ice, in: G. Papanicolaou (Ed.), Wave Propagation in Complex Media, IMA Volumes in Mathematics and its Applications, vol. 96, Springer, Berlin, 1997, pp. 75–94.
[21] K.M. Golden, M. Cheney, K.H. Ding, A.K. Fung, T.C. Grenfell, D. Isaacson, J.A. Kong, S.V. Nghiem, J. Sylvester, D.P. Winebrenner, IEEE Trans. Geosci. Remote Sensing 36 (5) (1998) 1655.
[22] L.G.E. Backstrom, H. Eicken, Capacitance probe measurements of brine volume and bulk salinity in first-year sea ice, Cold Regions Sci. and Technol. 46 (3) (2006) 167.
[23] D.J. Bergman, Phys. Rev. Lett. 44 (1980) 1285.
[24] G.W. Milton, Appl. Phys. Lett. 37 (1980) 300.
[25] K. Golden, G. Papanicolaou, Comm. Math. Phys. 90 (1983) 473.
[26] Z. Hashin, S. Shtrikman, J. Appl. Phys. 33 (1962) 3125.
[27] K.M. Golden, S.F. Ackley, V.I. Lytle, Science 282 (1998) 2238.
[28] W.F. Weeks, A.J. Gow, J. Geophys. Res. (Oceans) 85 (C2) (1980) 1137.
[29] E. Cherkaeva, K.M. Golden, Waves in Random Media 8 (4) (1998) 437.
[30] R.C. McPhedran, D.R. McKenzie, G.W. Milton, Appl. Phys. A 29 (1982) 19.
[31] R.C. McPhedran, G.W. Milton, Mater. Res. Soc. Symp. Proc. 195 (1990) 257.
[32] D.J. Bergman, Phys. Rep. C 43 (9) (1978) 377.
[33] D.J. Bergman, Ann. Phys. 138 (1982) 78.